Supplementary Information

Bio-inspired rotary flight of light-driven nanocomposite films

Dan Wang,[1,2#] Zhaomin Chen,[1#] Mingtong Li,[3#] Zhen Hou,[1] Changsong Zhan,[1] Qijun Zheng,[4] Dalei Wang,[1] Xin Wang,[1] Mengjiao Cheng,[2] Wenqi Hu,[3] Bin Dong,[1*] Feng Shi[2*] and Metin Sitti [3,5,6*]

[1]Institute of Functional Nano & Soft Materials (FUNSOM), Jiangsu Key Laboratory for Carbon-Based Functional Materials & Devices, State and Local Joint Engineering Laboratory for Novel Functional Polymeric Materials, Joint International Research Laboratory of Carbon-Based Functional Materials and Devices, Soochow University, Suzhou, Jiangsu 215123, China

[2]State Key Laboratory of Chemical Resource Engineering, Beijing Laboratory of Biomedical Materials, Beijing Advanced Innovation Center for Soft Matter Science and Engineering, Beijing University of Chemical Technology, Beijing, 100029, China

[3]Physical Intelligence Department, Max Planck Institute for Intelligent Systems, 70569 Stuttgart, Germany

[4]Department of Chemical Engineering, Monash University, Clayton, Vic 3800, Australia

[5]Institute for Biomedical Engineering, ETH Zürich, 8092 Zürich, Switzerland

[6]School of Medicine and College of Engineering, Koç University, 34450 Istanbul, Turkey

Table of content

Section S1. Supplementary videos

Supplementary Video 1. Light-driven rotary flying soft 'helicopter'.

Supplementary Video 2. Deformation process indicating the formation of the 'airscrew' structure.

Supplementary Video 3. Origination of the driving force, i.e., jet-propulsion.

Supplementary Video 4. Light-driven rotation in the vacuum environment.

Supplementary Video 5. Light-driven rotation with negative angle of attack.

Supplementary Video 6. Light-controlled flight to the left rear.

Supplementary Video 7. Light-controlled flight to the right rear.

Supplementary Video 8. Mimic of the vine maple seed: synchronous rotary-falling.

Supplementary Video 9. Wind dispersal of the light-driven 'helicopter'.

Supplementary Video 10. Light-driven 'helicopter' flying across a trench.

Supplementary Video 11. Light-driven 'helicopter' flying over a barrier.

Section S2. Supplementary table

Supplementary Table 1. Comparison of the rotational speed of photoactuators with different shapes and driving mechanisms.

Photoactuator material	**Shape**	**Rotation speed (rpm)**	**Mechanism**	**Ref.**
Graphene/agar/silk fibroin nanocomposite	Airscrew	7200	Jet propulsion	This work
Carbonized PDMS	Microgear	94.2	Marangoni effect	1
Carbon/SU-8	Microgear	300	Marangoni effect	2
Pyrolytic graphite	Disk	200	Magnetic susceptibility change	3
Ink/PET/acrylic	Light mill	19	Wing-flapping	4

Section S3. Supplementary figures.

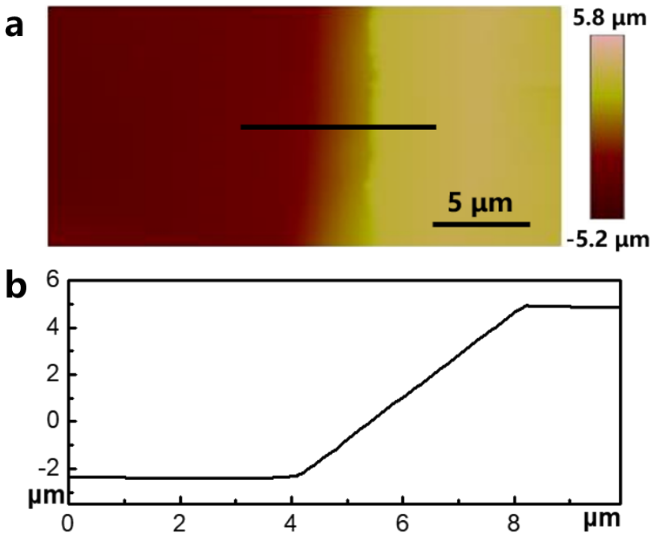

Figure S1. (a) The Atomic force microscopy (AFM) image showing the edge of the microchannel on the surface of the graphene/agar/silk fibroin nanocomposite film. The corresponding section analysis of (a) is shown in (b).

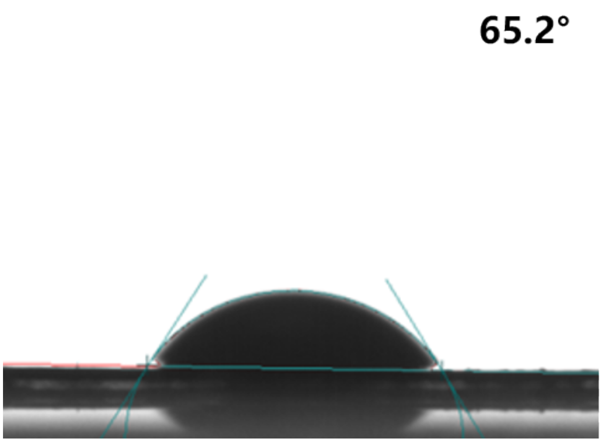

Figure S2. The water contact angle on the graphene/agar/silk fibroin nanocomposite film.

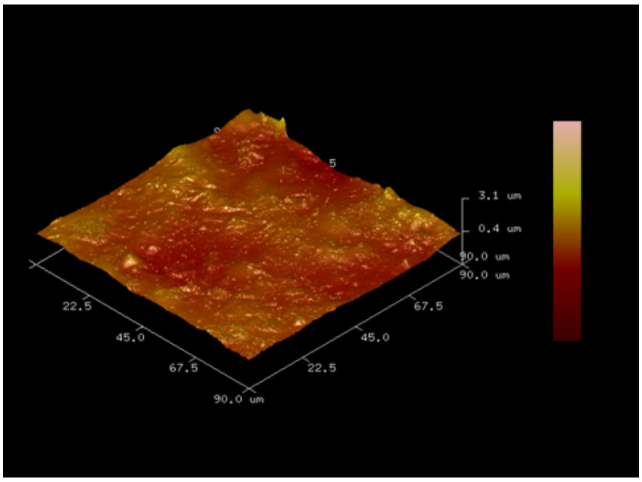

Figure S3. The AFM image showing the 3D surface morphology of the graphene/agar/silk fibroin nanocomposite film.

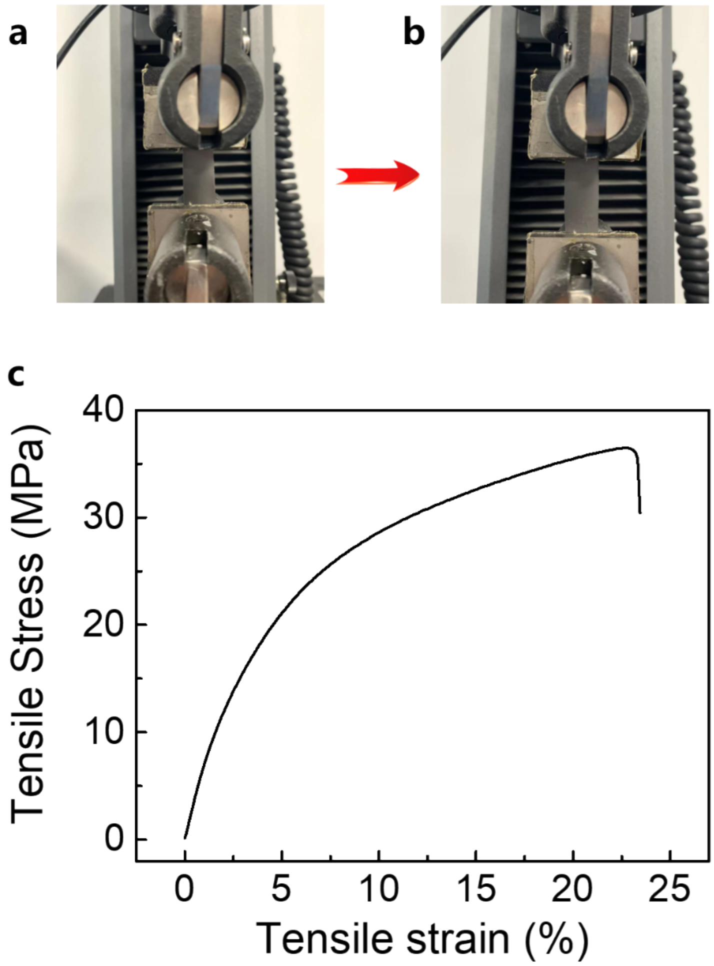

Figure S4. A stripe-shaped graphene/agar/silk fibroin nanocomposite film (a) before and (b) after stretching. (c) Tensile stress-strain curve of the graphene/agar/silk fibroin nanocomposite film.

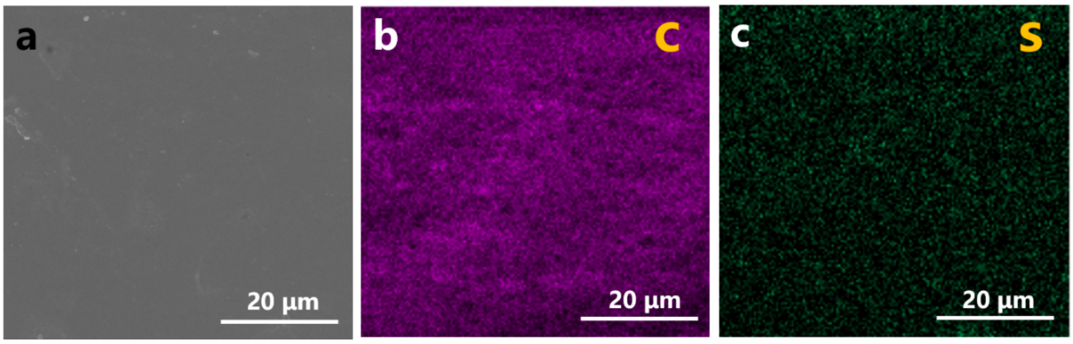

Figure S5. (a) Scanning electron microscopy (SEM) image showing the surface morphology of the graphene/agar/silk fibroin nanocomposite film. Energy-dispersive X-ray (EDX) analysis of the graphene/agar/silk fibroin nanocomposite film showing the homogeneous distribution of (b) carbon and (c) sulfur elements.

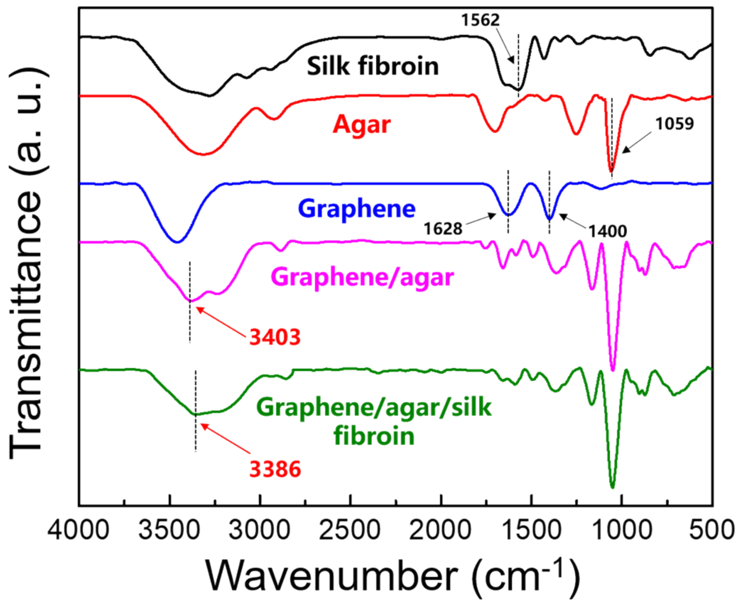

Figure S6. Fourier transform infrared spectroscopy (FTIR) spectra of silk fibroin (black curve), agar (red curve), graphene (blue curve), graphene/agar film (purple curve) and the graphene/agar/silk fibroin nanocomposite film (green curve).

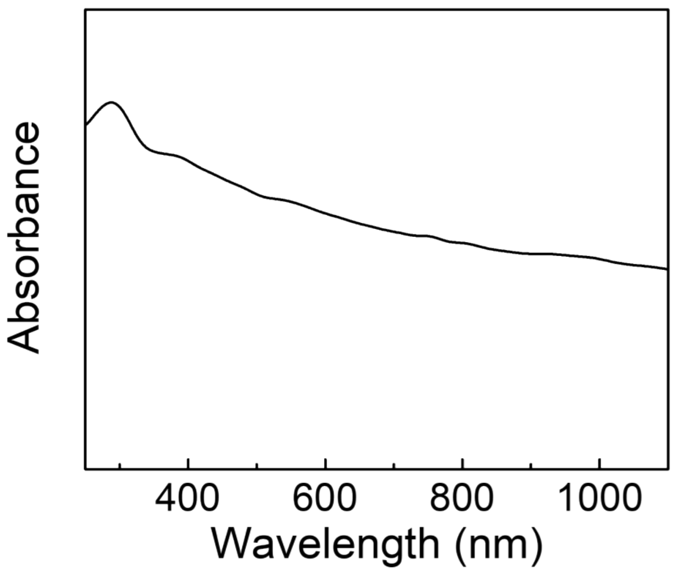

Figure S7. The UV-Vis-NIR spectrum of the graphene/agar/silk fibroin nanocomposite film.

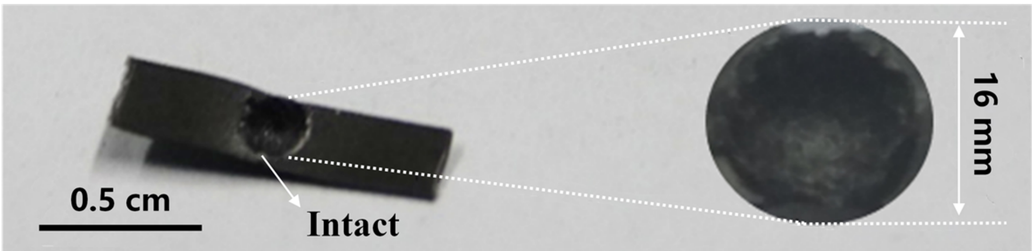

Figure S8. CCD images showing the sectioned protrusion which indicates the hollow interior structure. Note that the protrusion only expands to one side of the film and the opposite side remains intact.

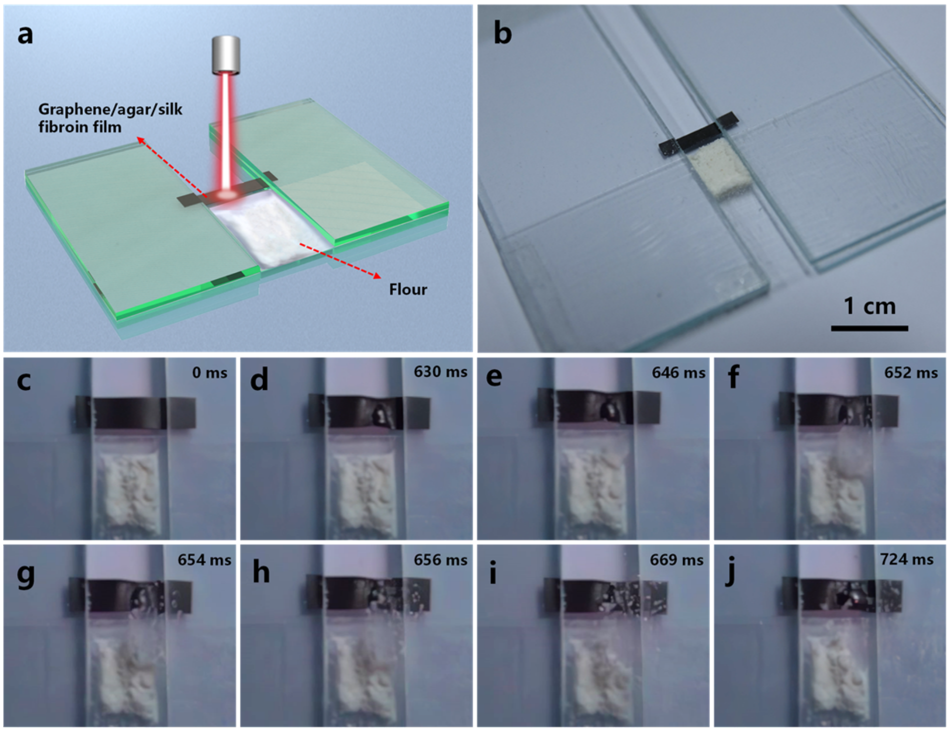

Figure S9. (a) Schematic illustration indicating the experimental setup for the verification of the jet propulsion. Time lapse images obtained from Supplementary Video 3 showing the graphene/agar/silk fibroin nanocomposite film (b,c) before and (d-j) after light actuation.

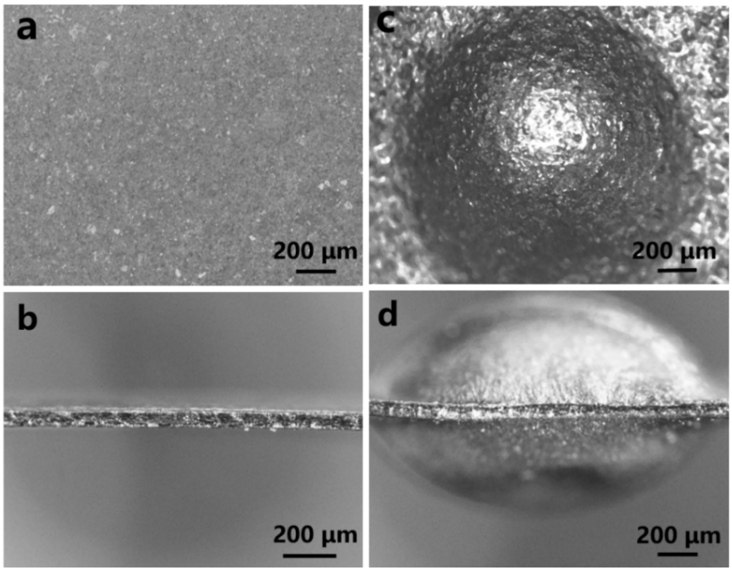

Figure S10. Microscopic images showing the structure of the graphene/agar/silk fibroin nanocomposite film (a-b) before and (c-d) after light actuation: (a,c) top view and (b,d) cross-sectional view. There are negligible changes at the film edge where the jet propulsion occurs.

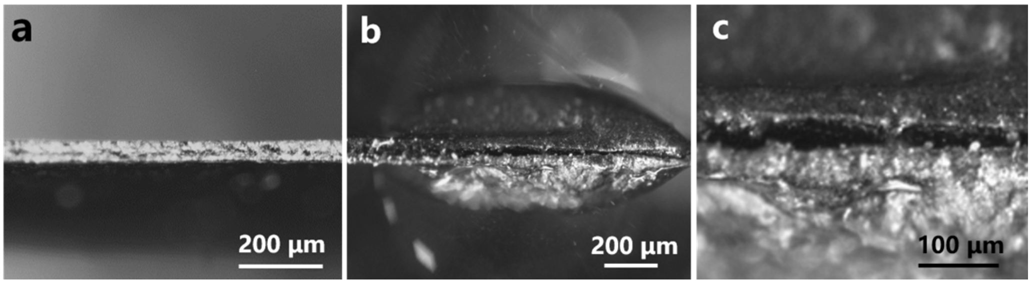

Figure S11. Optical microscopic images showing the cross-sectional view of the graphene/agar nanocomposite film (in the absence of silk fibroin) (a) before and (b) after light actuation. (c) Enlarged microscopic image showing the split at the film edge after the jet propulsion.

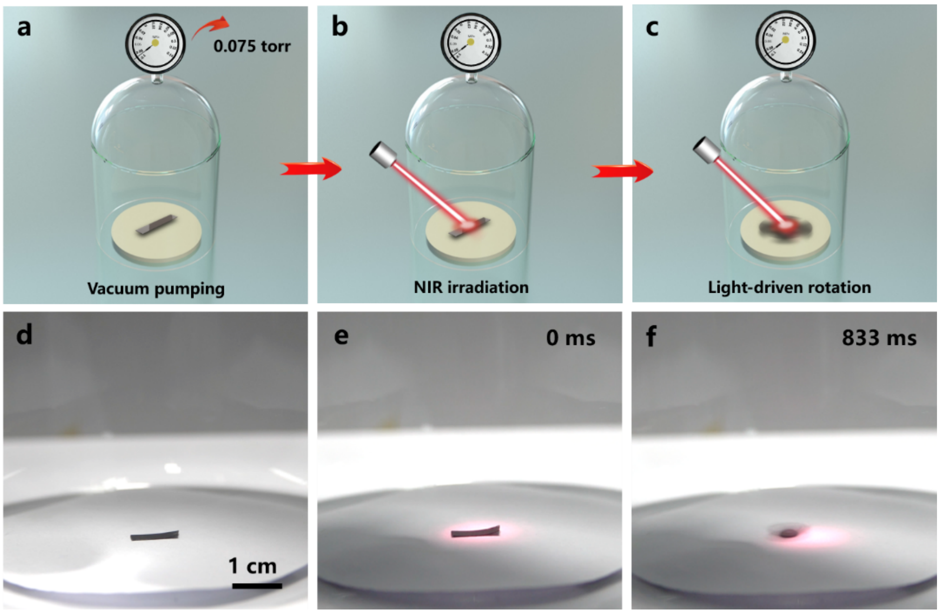

Figure S12. (a-c) Schematic illustration and (d-f) the corresponding time lapse images obtained from Supplementary Video 4 indicating the light-driven rotation of the graphene/agar/silk fibroin nanocomposite film in vacuum (0.075 torr).

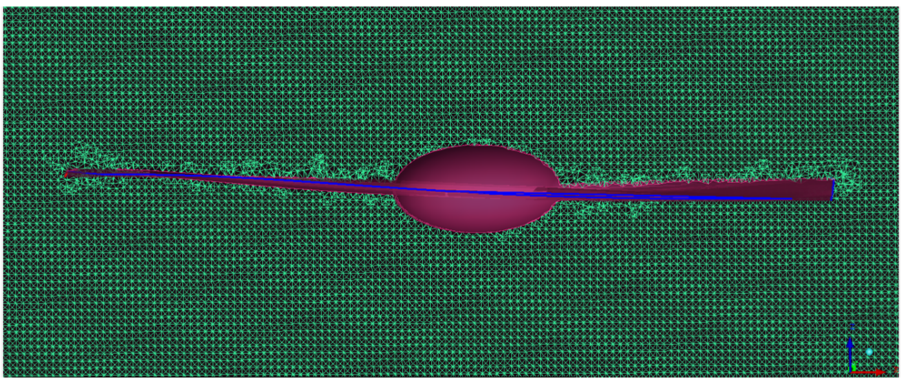

Figure S13. Computation mesh used for the computational fluid dynamics (CFD) simulation.

The 3D models and computational domains at different angle of attack are created using the CFD module. During this process, the whole computational domain is divided by unstructured mesh. The computational mesh of a 10 mm × 2 mm × 60 µm (length × width × thickness) sized film with an angle of attack of 15° is shown in Supplementary Fig. 13. The computational boundary (x, y and z) domains are set as 5, 2 and 10 times of the length, width and thickness of the film, respectively (the number of meshes is 5,000,000). The boundary conditions are set as follows: The inlet condition is set as the velocity inlet, the outlet condition is set as a zero-gradient pressure outlet and a uniform free incoming velocity is used. The wall boundary condition with no slip and no penetration is used for the film surface. The number of boundary mesh layers is 10, the thickness of the first layer is 0.001 times of the thickness of the film.

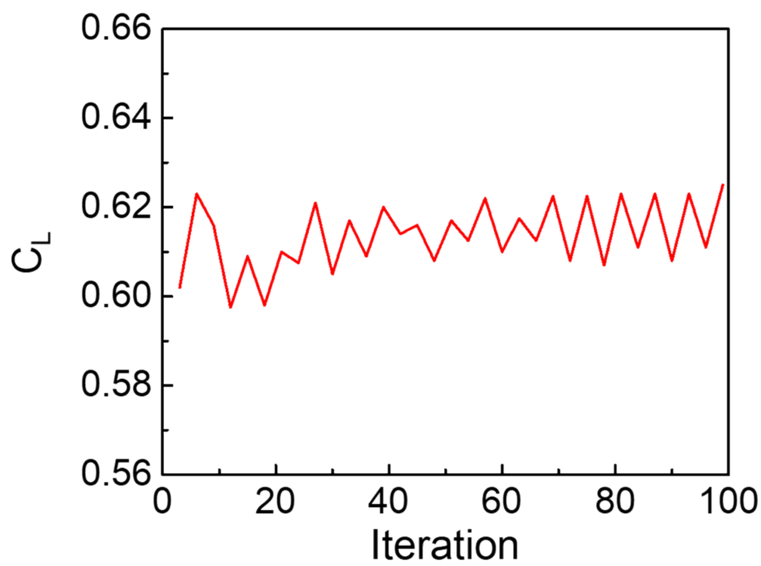

Figure S14. Lift coefficient (C_L) of the light-driven soft 'helicopter'.

The k-epsilon model in Fluent module is used, the fluid is set as air (the air flow rate is set as 10 m/s) and the characteristic area of the reference value is 0.23 cm^2. Accordingly, the average simulated value of the lift coefficient (C_L) based on the k-epsilon model is 0.61, as shown in Supplementary Fig. 14. Therefore, the lift force can be calculated to be 4.12×10^{-4} N, which is in the same order of magnitude as the lift force calculated based on Equation 1 (1.44×10^{-4} N), thus demonstrating that the rotation-induced lift force is likely to be the driving force for flight.

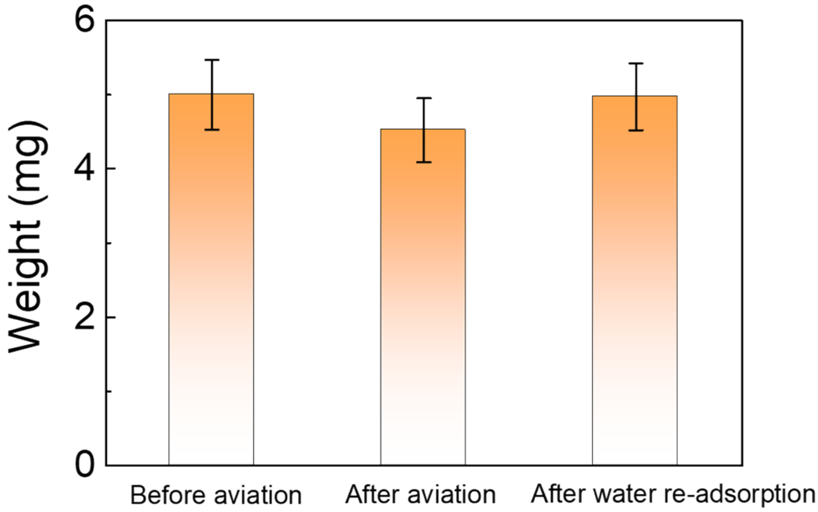

Figure S15. The weight variation of the graphene/agar/silk fibroin nanocomposite film before light-driven flight, after light-driven flight and after water re-adsorption.

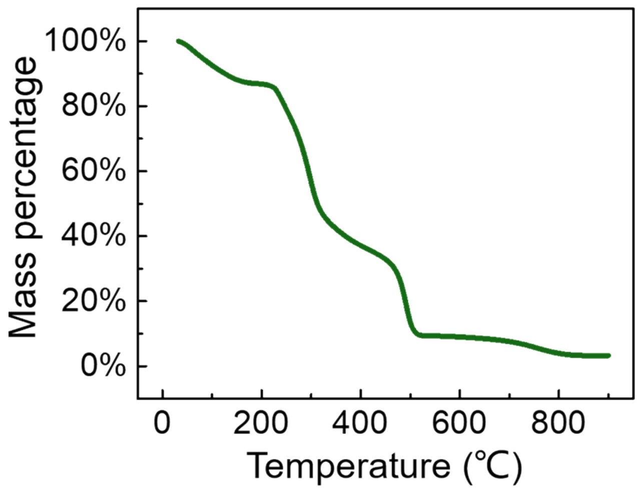

Figure S16. The thermogravimetric analysis (TGA) of the graphene/agar/silk fibroin nanocomposite film.

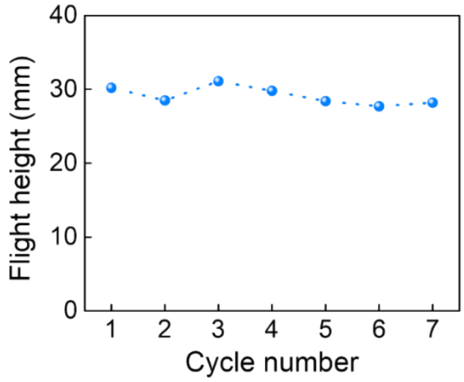

Figure S17. The repeatability of the light-driven flight of the 'helicopter' under 0.3 W/cm^2 repetitive light actuation.

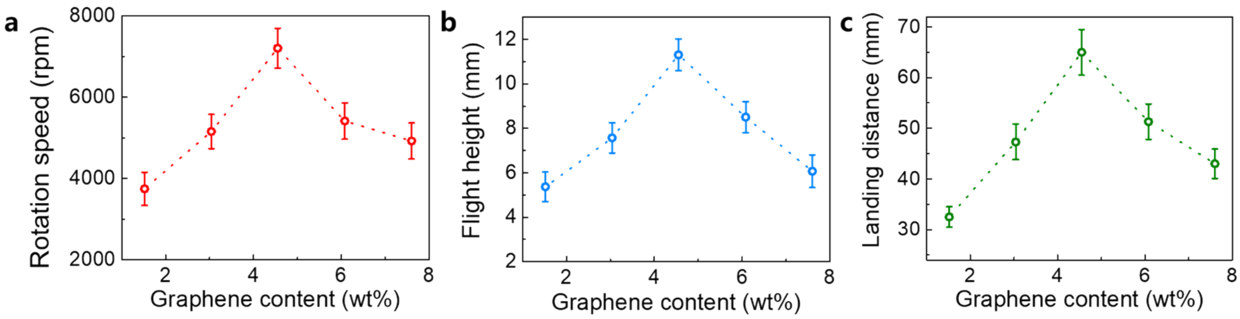

Figure S18. The influence of the graphene content on (a) the rotational speed, (b) the flight height, and (c) the landing distance of the light-driven 'helicopter'.

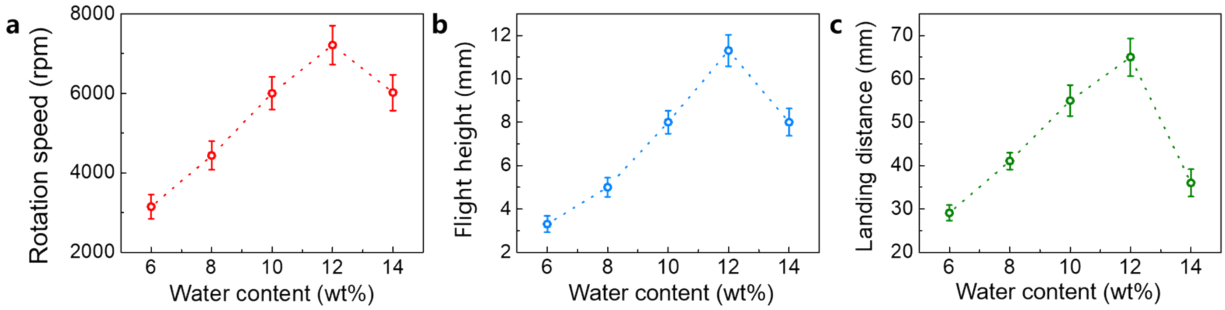

Figure S19. The influence of the water content on (a) the rotational speed, (b) the flight height, and (c) the landing distance of the light-driven 'helicopter'.

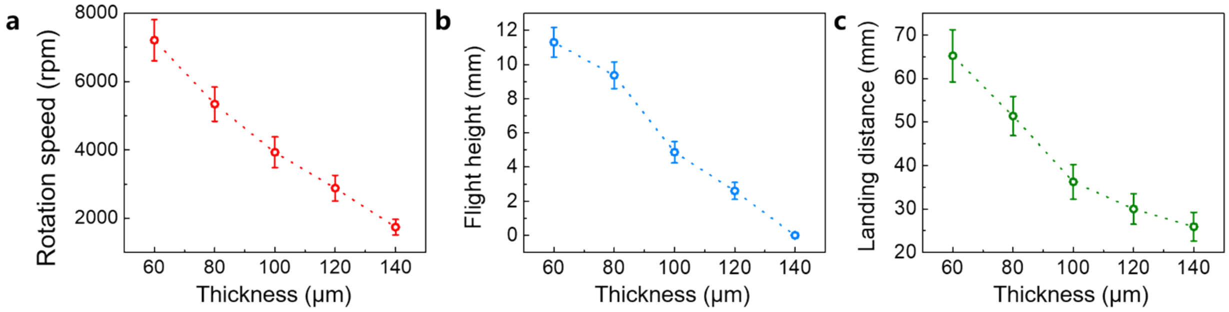

Figure S20. The influence of the thickness of the nanocomposite film on (a) the rotational speed, (b) the flight height, and (c) the landing distance of the light-driven 'helicopter'.

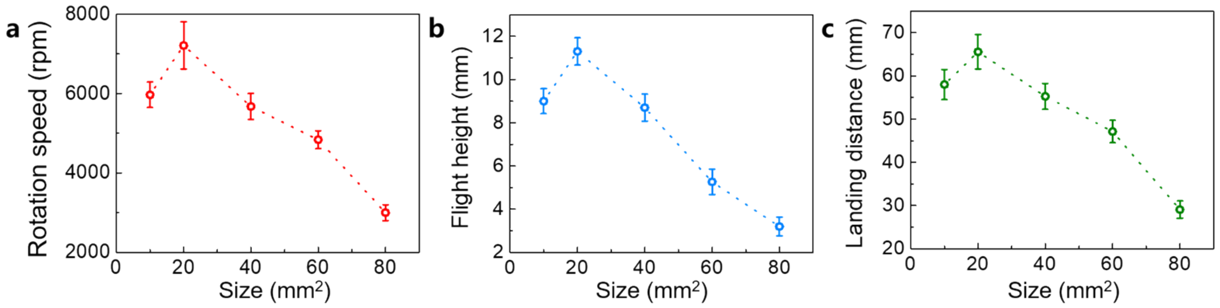

Figure S21. The influence of size of the nanocomposite film on (a) the rotational speed, (b) the flight height, and (c) the landing distance of the light-driven 'helicopter'.

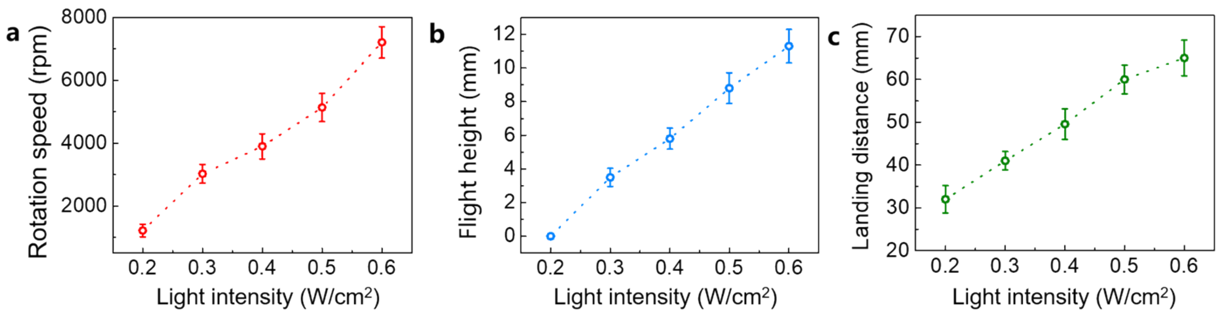

Figure S22. The influence of the irradiation light intensity on (a) the rotational speed, (b) the flight height, and (c) the landing distance of the light-driven 'helicopter'.

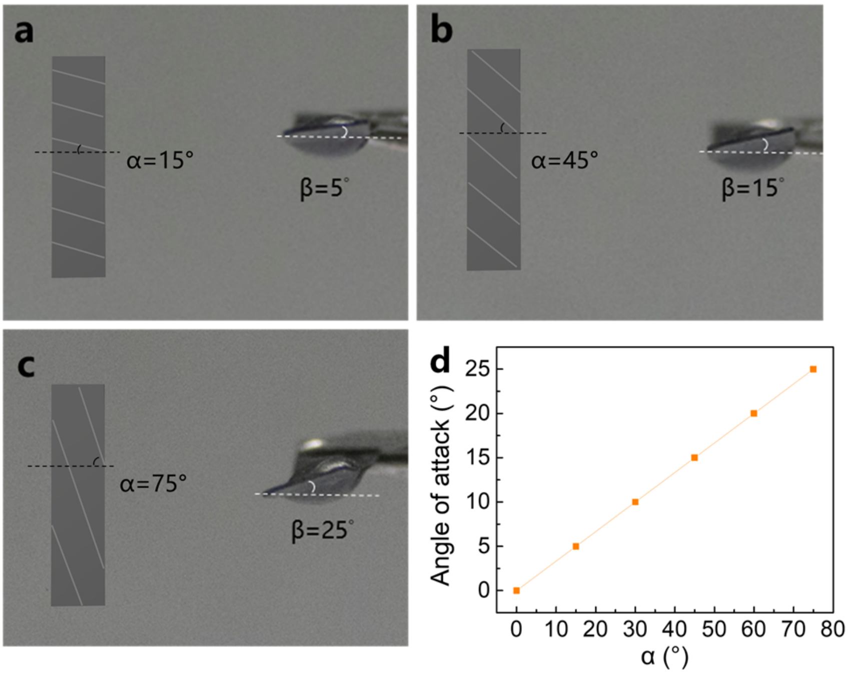

Figure S23. (a-c) CCD images showing the angle of attack (β) of the light-driven 'helicopter' could be realized by controlling the alignment angle (α) of the micropatterns (with respect to the short axis of the nanocomposite film). (d) Angle of attack depends on the alignment angle of the micropatterns (α).

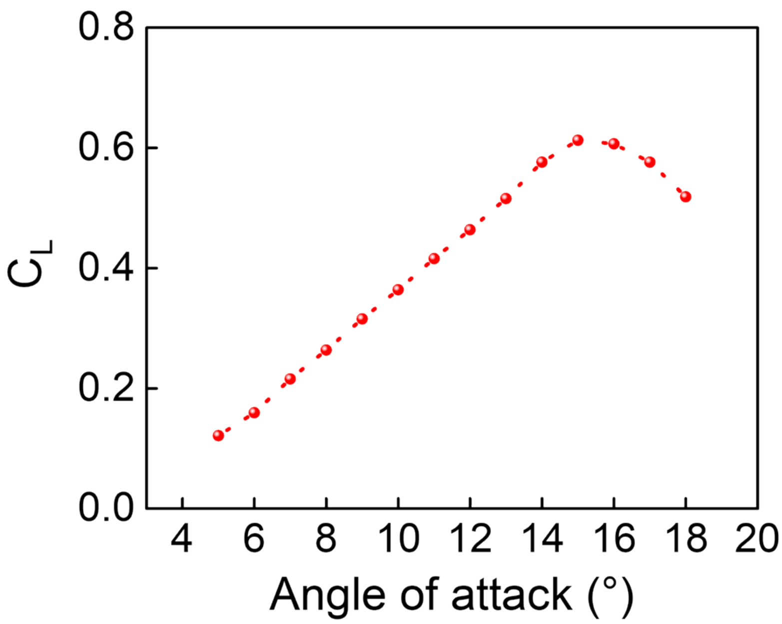

Figure S24. The CFD simulation showing the influence of the angle of attack on the lift coefficient (C_L). We have studied the effect of angle of attack on C_L based on the simulation. As shown in

Supplementary Fig. 24, C_L first increases gradually with the increase of the angle of attack then decreases. The optimal angle of attack is 15°, at which C_L reaches the maximum value of 0.61.

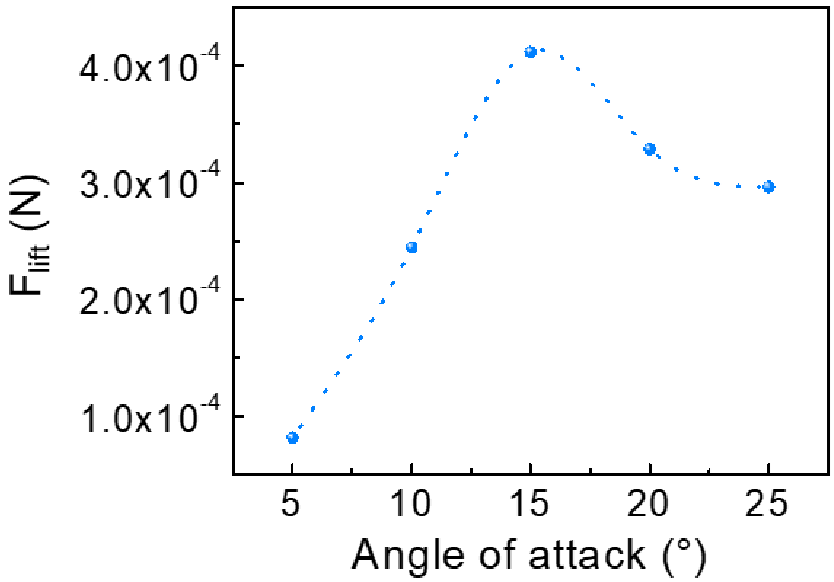

Figure S25. The CFD simulation showing the influence of angle of attack on the lift force (F_{lift}).

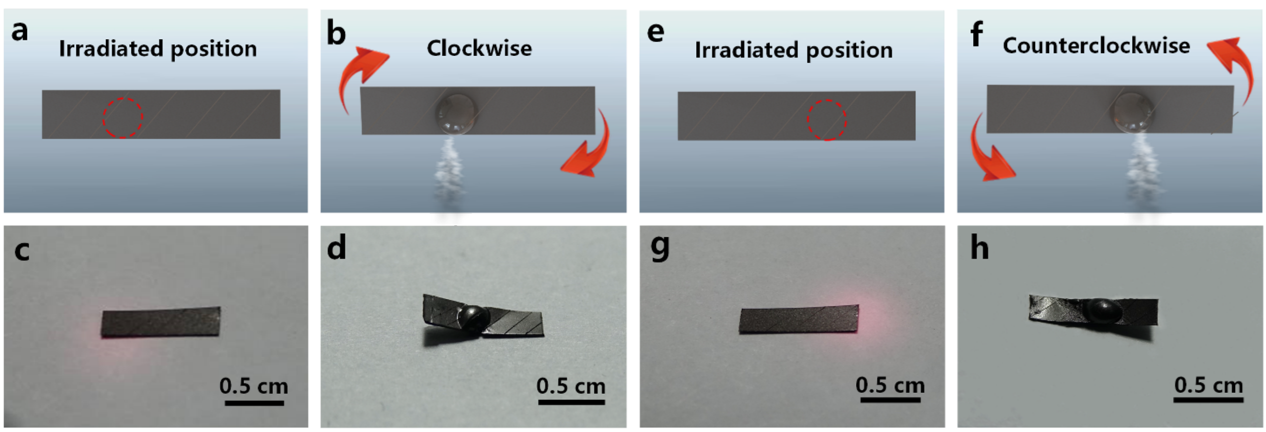

Figure S26. Schematic illustration and CCD images showing the controlled (a-d) clockwise and (e-h) counterclockwise rotation which is realized by controlling the position of the jet propulsion. (a-d) The jet propulsion at the lower left part of the film induces the clockwise rotation, while (e-h) that at the lower right part of the film leads to the counterclockwise rotation.

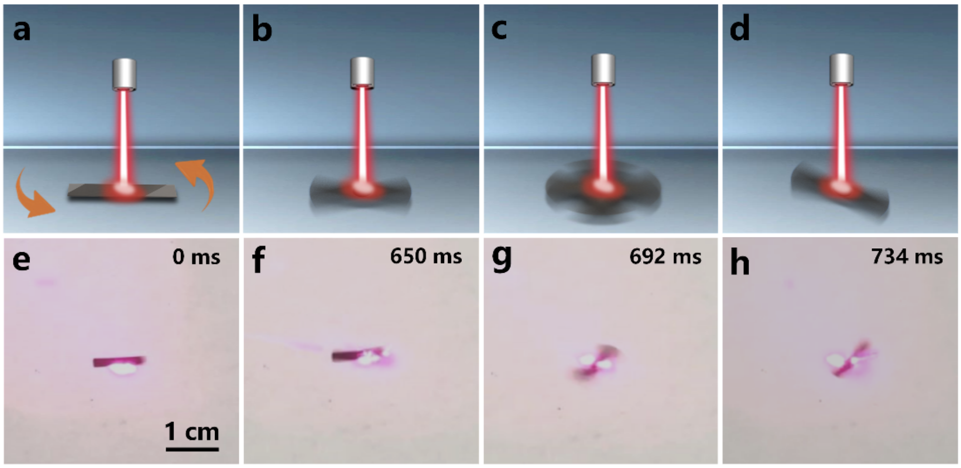

Figure S27. (a-d) Schematic illustration and (e-h) the corresponding time lapse images obtained from Supplementary Video 5 showing the light-driven graphene/agar/silk fibroin nanocomposite film only rotates when the angle of attack is negative.

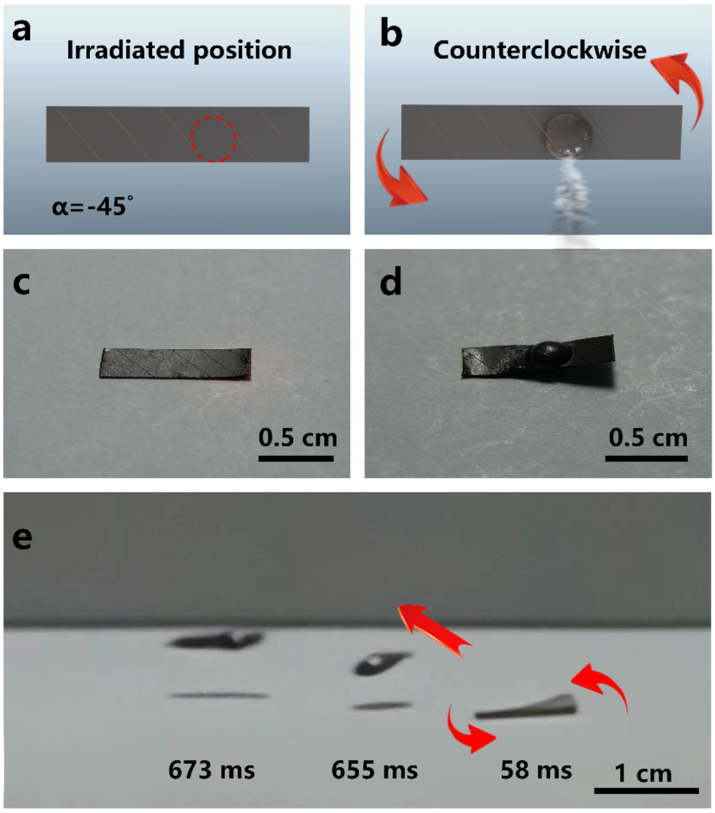

Figure S28. (a,b) Schematic illustration and (c,d) the CCD images showing that, by changing the alignment angle of the micropatterns (α) (from 45° in case of Supplementary Fig. 26 to -45°), the counterclockwise rotation could result in the flying motion. (e) Overlaid CCD images showing the counterclockwise rotation could also lead to the flying motion.

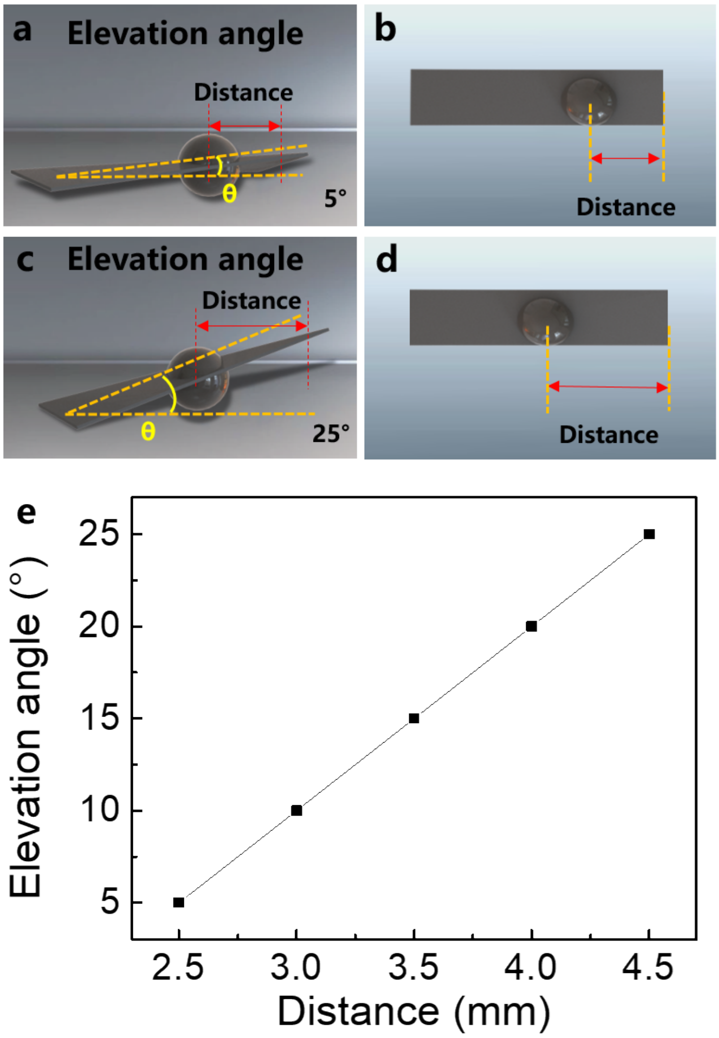

Figure S29. Schematic illustration showing the elevation angle (θ) of (a,b) 5° and (c,d) 25° which are adjusted by controlling the position of the protrusion. (e) Elevation angle could be controlled by controlling the distance away from the end of the film.

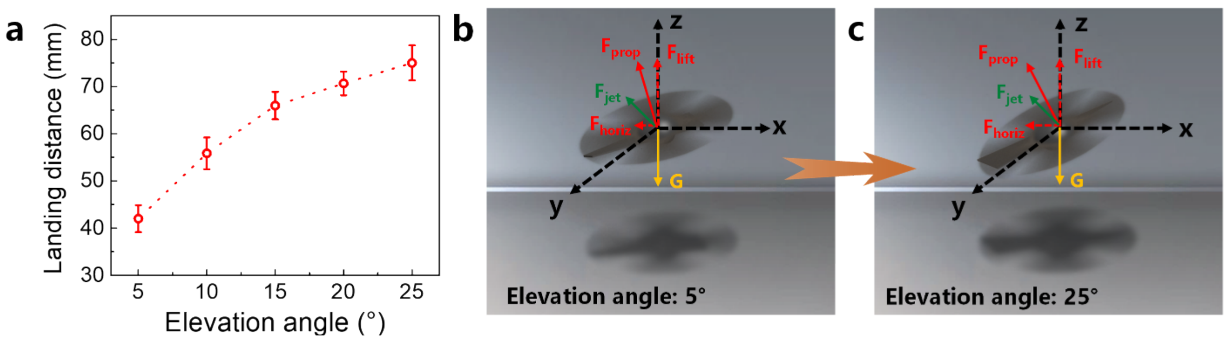

Figure S30. (a) Landing distance as a function of the elevation angle of the light-driven 'helicopter'. Force analysis of the light-driven 'helicopter' with elevation angle of (b) 5° and (c) 25°, respectively.

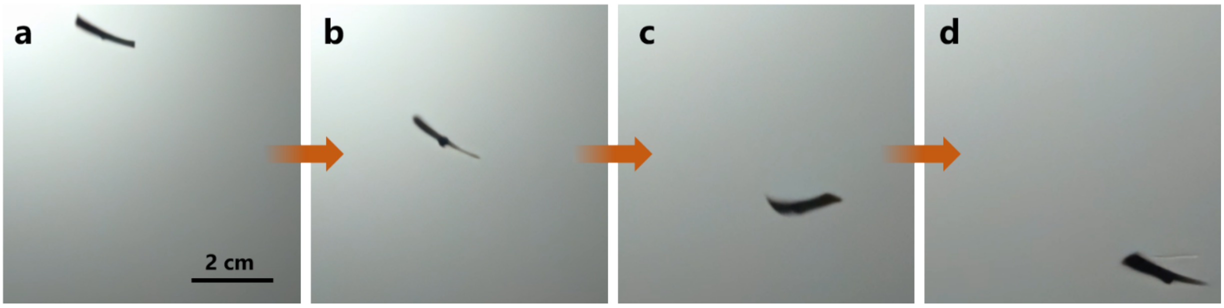

Figure S31. (a-d) Time lapse images within 74 ms obtained from Supplementary Video 9 showing the apparent horizontal displacement of the graphene/agar/silk fibroin nanocomposite film during the rotary-falling process in the presence of a crosswind (the wind speed is 3 m/s).

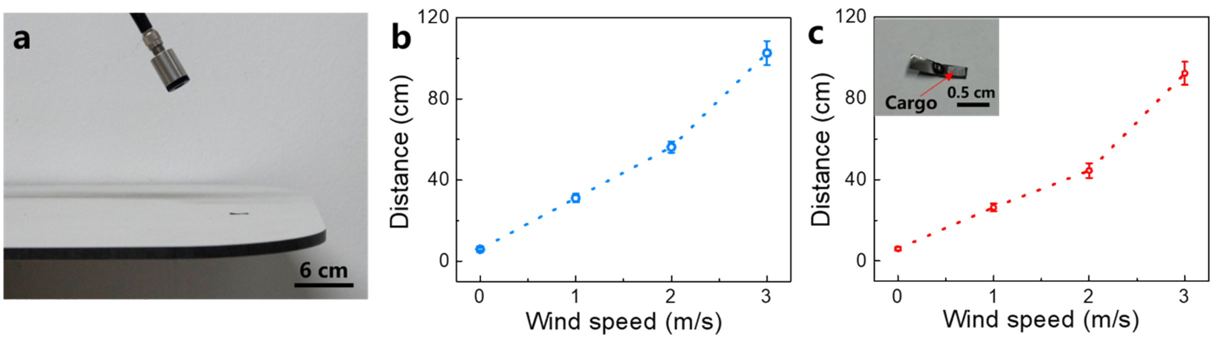

Figure S32. (a) CCD image showing the experimental setup for the 'helicopter' released upon light actuation. (b) The wind dispersal distance of the light-driven 'helicopter' under different wind speeds. (c) The wind dispersal distance of the light-driven 'helicopter' loaded with a cargo (with a weight of 0.1 mg) under different wind speeds. Inset: CCD image indicating the light-driven 'helicopter' with a model cargo consisting of paper attached onto its airscrew structure.

References

1. Wang, W., Liu, Y., Liu, Y., Han, B., Wang, H., Han, D., Wang, J., Zhang, Y. & Sun, H. Direct laser writing of superhydrophobic PDMS elastomers for controllable manipulation via marangoni effect. *Adv. Funct. Mater.* **27**, 1702946 (2017).

2. Maggi, C., Saglimbeni, F., Dipalo, M., De Angelis, F. & Di Leonardo, R. Micromotors with

asymmetric shape that efficiently convert light into work by thermocapillary effects. *Nat. Commun.* **6**, 7855 (2015).

3. Kobayashi, M. & Abe, J. Optical motion control of maglev graphite. *J. Am. Chem. Soc.* **134**, 20593-20596 (2012).

4. Li, J., Zhang, R., Mou, L., Jung de Andrade, M., Hu, X., Yu, K., Sun, J., Jia, T., Dou, Y., Chen, H., Fang, S., Qian, D. & Liu, Z. Photothermal bimorph actuators with in-built cooler for light mills, frequency switches, and soft robots. *Adv. Funct. Mater.* **29**, 1808995 (2019).